



Article

Thrombin Generation Thresholds for Coagulation Initiation under Flow

Anass Bouchnita ^{1,2,*}, Kanishk Yadav ² , Jean-Pierre Llored ³, Alvaro Gurovich ⁴  and Vitaly Volpert ^{5,6}¹ Department of Mathematical Sciences, The University of Texas at El Paso, El Paso, TX 79968, USA² Bioinformatics Program, The University of Texas at El Paso, El Paso, TX 79968, USA³ Ecole Centrale Casablanca, Ville Verte Bouskoura, Casablanca 20000, Morocco;

jeanpierre.llored@centrale-casablanca.ma

⁴ Department of Physical Therapy and Movement Sciences, The University of Texas at El Paso, El Paso, TX 79968, USA; agurovich@utep.edu⁵ Institut Camille Jordan, UMR 5208 CNRS, University Lyon 1, 69622 Villeurbanne, France; volpert@math.univ-lyon1.fr⁶ S.M. Nikolsky Mathematical Institute, Peoples Friendship University of Russia (RUDN University), 6 Miklukho-Maklaya St., Moscow 117198, Russia

* Correspondence: abouchnita@utep.edu

Abstract: In veins, clotting initiation displays a threshold response to flow intensity and injury size. Mathematical models can provide insights into the conditions leading to clot growth initiation under flow for specific subjects. However, it is hard to determine the thrombin generation curves that favor coagulation initiation in a fast manner, especially when considering a wide range of conditions related to flow and injury size. In this work, we propose to address this challenge by using a neural network model trained with the numerical simulations of a validated 2D model for clot formation. Our surrogate model approximates the results of the 2D simulations, reaching an accuracy of 94% on the test dataset. We used the trained artificial neural network to determine the threshold for thrombin generation parameters that alter the coagulation initiation response under varying flow speed and injury size conditions. Our model predictions show that increased levels of the endogenous thrombin potential (ETP) and peak thrombin concentration increase the likelihood of coagulation initiation, while an elevated time to peak decreases coagulation. The lag time has a small effect on coagulation initiation, especially when the injury size is small. Our surrogate model can be considered as a proof-of-concept of a tool that can be deployed to estimate the risk of bleeding in specific patients based on their Thrombin Generation Assay results.

Keywords: mathematical modeling; deep learning; numerical simulations; blood clots; bleeding; neural networks



Citation: Bouchnita, A.; Yadav, K.; Llored, J.-P.; Gurovich, A.; Volpert, V. Thrombin Generation Thresholds for Coagulation Initiation under Flow. *Axioms* **2023**, *12*, 873. <https://doi.org/10.3390/axioms12090873>

Academic Editors: Mikhail Kuptsov and Sergey Leontyevich Yablochnikov

Received: 9 August 2023

Revised: 7 September 2023

Accepted: 8 September 2023

Published: 12 September 2023



Copyright: © 2023 by the authors. Licensee MDPI, Basel, Switzerland. This article is an open access article distributed under the terms and conditions of the Creative Commons Attribution (CC BY) license (<https://creativecommons.org/licenses/by/4.0/>).

1. Introduction

Blood coagulation is a complex process that involves the activation of multiple biochemical pathways leading to the formation of a blood clot. This process is highly regulated and involves the interplay of several factors, including shear stress, flow rate, and the presence of platelets and other clotting factors. Recent studies have shown that the coagulation response displays a threshold-like behavior in response to changes in flow intensity [1] and injury size [2].

In venous conditions, the rate and the extent of clot formation depend on various factors, including the intensity and duration of exposure to blood circulation. Blood flow influences clot initiation and growth in multiple ways. First, it transports the coagulation zymogens to the site of the injury, accelerating the onset of coagulation. At the same time, high shear flow removes activated coagulation factors and limits the development of the clot. The size of the injury can significantly affect the growth of a blood clot [3]. A larger injury size not only increases the likelihood of clot initiation, but typically results in a larger,

more robust clot. This is because a larger injury will expose more tissue factor, which can further activate the coagulation cascade and increase the rate of thrombin generation.

Blood coagulability is a crucial factor that affects the process of clot initiation and growth under flow. Along with flow stasis and endothelial injury, hypercoagulability constitutes the three pillars of the Virchow triad [4]. However, measuring the coagulability of blood accurately is a challenging task, as it is usually conducted using *in vitro* tests that do not mimic the *in vivo* conditions of clot formation. One widely accepted method for assessing blood coagulability is the Thrombin Generation Assay (TGA) [5]. This *in vitro* test measures the ability of blood to form clots, and specifically the generation of thrombin, which is a key enzyme involved in the coagulation process. The assay measures the amount of thrombin generated over time in response to a stimulus, such as tissue factor, and provides information on the coagulation status of an individual's blood. Thus, it can be used to assess the risk of bleeding or thrombosis, monitor anticoagulant therapy, and study the mechanisms of blood clotting disorders.

Ordinary differential equation (ODE) models can be used to describe the kinetics of thrombin generation [6–10]. These coagulation models aim to describe the concentration evolution of various coagulation factors during the clotting process. However, there are concerns regarding the extent to which these models accurately represent the physiological mechanisms underlying blood coagulation, particularly for clinical decision-making. One notable limitation is the simplification of reactions within the coagulation cascade, neglecting several biochemical pathways. For instance, the protein C-independent inhibitory action of protein S, which has been shown to play a crucial role in *in vivo* experiments [11], is often overlooked. Additionally, existing thrombin generation models exhibit significant variations in the kinetic constants considered, largely due to disparities in the experimental conditions used for their measurement [12]. Despite these limitations, these models can be calibrated to replicate experimentally observed thrombin generation curves, albeit without fully capturing all of the involved mechanisms.

However, the interpretation of the results of the TGA is challenging, as it provides us with a curve quantifying the concentration of generated thrombin over time. This curve can be characterized by four distinct parameters: (i) the lag time, (ii) the peak thrombin concentration, (iii) the time to peak, and (iv) the endogenous thrombin potential (ETP). The lag time refers to the time required for the initial amount of thrombin to generate. The peak thrombin concentration indicates the highest concentration of thrombin generated. The time to peak defines the velocity of thrombin generation. It corresponds to the moment when thrombin generation reaches its peak. The area under the curve, referred to as the endogenous thrombin potential (ETP), represents the net amount of thrombin generated by the test plasma. While a low ETP and peak concentration suggest an elevated risk of bleeding, it is hard to predict the actual hemostatic response using solely these parameters, especially when considering *in vivo* flow intensity and injury size conditions. Further, the overall experience with the thrombin generation test as a surrogate measure of hemostatic efficacy is still rather limited, and there are no guidelines on the interpretation of the results of these assays.

Various approaches have been employed by mathematical modelers to describe thrombus formation under flow in both normal and pathological conditions. One such method is continuum-based modeling, which is a powerful tool to study thrombus formation in complex geometries and under different flow conditions. These models typically use the Navier–Stokes equations to describe blood flow and rely on partial differential equations to model the distribution of blood components. The coupling between the two is achieved by considering fibrin polymer as an influencing factor for blood viscosity, or by treating the clot as a porous medium whose viscosity is dependent on fibrin density [13–18]. Continuum-based models are also suitable for studying thrombus formation in arterial flow and complex geometries such as aneurysms. Mixture theory is used in some continuous models to capture the interplay between platelets, plasma, red blood cells (RBCs), and the clot [19–21]. Another widely used class of models for describing thrombus growth under

flow is multiscale modeling, which combines continuous and discrete representations of the underlying mechanisms [22–28]. Multiscale models allow the tracking of individual blood cells and provide a more accurate description of cell-based processes such as platelet deposition, transport, and aggregation, as the mechanisms involved span multiple scales of space and time.

However, numerical simulations come at an expensive computational cost, which limits their potential for the systematic exploration of a complex system such as thrombus formation under flow. Further, using simulations to predict the coagulation response of specific patients under a wide range of flow and injury size conditions would require many hours to a few days, while clinical intervention relies on time-sensitive decision making. On the other hand, a data-driven approach such as machine learning can be used to evaluate the risk of prothrombotic diseases using patient information related to comorbidities and lifestyle [29,30]. While this approach can provide accurate and timely predictions, its output usually lacks interpretability, which poses a challenge to their adoption by healthcare practitioners. Recently, we have developed a method that combines deep learning with a mathematical model to make fast and explainable predictions on the effect of anticoagulants [31], as well as the risk of thrombosis in COVID-19 patients [32].

Identifying the features of thrombin generation curves that prevent coagulation initiation under varying flow and injury conditions is a challenging but highly important problem. Solving it would allow health practitioners to rely on thrombin generation assays results to make clinical decisions [33,34]. In this work, we propose to explore this question using a new approach that combines mathematical modeling with machine learning. In particular, we propose to identify the thrombin generation thresholds that prevent coagulation initiation under varying flow and injury size conditions. We utilized a deep learning model that we trained using numerical simulations of a computational fluid dynamics (CFD) model for coagulation initiation under flow. After validating this CFD model against microfluidics experiments, we took advantage of our high-performance computing resources to conduct 7675 simulations, describing the clotting initiation and growth. In each of these simulations, the model parameters related to coagulability, injury size, and flow pressure difference were randomly sampled, and the thrombin generation parameters were calculated. The obtained dataset was used to train an artificial neural network, which is able to predict the initiation of coagulation based on the thrombin generation parameters in addition to the injury size and flow intensity. We evaluated the accuracy and performance of the surrogate model. We then used the surrogate model for a fast exploration of thrombin generation thresholds that alter coagulation under various flow and injury size conditions. We conclude this paper by discussing how this approach can be further validated and deployed in clinical settings to help health care providers identify and manage patients with coagulation disorders on a case-to-case basis.

2. Determining Thrombin Generation Thresholds under Flow

2.1. Mathematical Modeling of Clot Formation under Flow

2.1.1. Spatio-Temporal Distribution of Clotting Factors

We incorporate diffusion and transport by flow in the previously introduced model of thrombin generation [13]. This thrombin generation model was derived from a more complete model as shown in Appendix A.1 using fast equilibrium approximations. We describe the spatial distributions of factor Xa (U), thrombin (T), and prothrombin (P) as follows:

$$\frac{\partial U}{\partial t} + \nabla \cdot (\mathbf{u}U - D_t \nabla U) = (K_1 + K_2T + K_3T^2)(U^0 - U) - K_4U, \quad (1)$$

$$\frac{\partial T}{\partial t} + \nabla \cdot (\mathbf{u}T - D_t \nabla T) = (K_5U + K_6T + K_7T^2 + K_8T^3)P - K_9T, \quad (2)$$

$$\frac{\partial P}{\partial t} + \nabla \cdot (\mathbf{u}P - D_t \nabla P) = -(K_5U + K_6T + K_7T^2 + K_8T^3)P. \quad (3)$$

Here, the second terms on the left-hand side of the three equations describe the diffusion of these three proteins and their transport by blood plasma. For prothrombin, we set an initial and left boundary condition of $P = P_0$ and a zero-flux condition at the rest of the boundaries. We consider a zero-flux boundary conditions for thrombin and factor Xa everywhere, except for the injury site where we consider the following condition describing the activation of factor X by the complex TF-FVIIa during the initiation stage [14]:

$$\frac{\partial U}{\partial \mathbf{n}} = \frac{K_1(U^0 - U)}{D(1 + \beta_1(U^0 - U))}. \quad (4)$$

Here, U^0 represents the concentration of factor X in the bloodstream. Next, we add the equations for fibrin polymerization:

$$\frac{\partial F_g}{\partial t} + \nabla \cdot (\mathbf{u} F_g - D_f \nabla F_g) = -K_{11} T F_g, \quad (5)$$

$$\frac{\partial F}{\partial t} + \nabla \cdot (\mathbf{u} F - D_f \nabla F) = K_{11} T F_g - K_{12} F, \quad (6)$$

$$\frac{\partial F_p}{\partial t} = K_{12} F. \quad (7)$$

Here, F_g , F , and F_p describe the concentrations of fibrinogen, fibrin, and fibrin polymer, respectively. Fibrin polymer does not diffuse and is not transported by flow. Therefore, we do not consider diffusion and advection terms in the equation for fibrin polymer. We set the inlet and initial condition of $F_g = F_{g0}$ for fibrinogen. The zero-flux condition is set at the rest of the boundaries. The same condition is applied everywhere for fibrin.

2.1.2. Blood Plasma and Its Interplay with the Clot

To reproduce the microfluidics experiments [1], we model blood plasma as a Newtonian incompressible fluid as follows:

$$\rho \frac{\partial \mathbf{u}}{\partial t} + \rho (\mathbf{u} \cdot \nabla) \mathbf{u} = -\nabla p + \mu \Delta \mathbf{u} - \frac{\mu}{K_f} \mathbf{u}, \quad \nabla \cdot \mathbf{u} = 0, \quad (8)$$

where \mathbf{u} is the flow velocity, p is the pressure, ρ is the density of the blood, and μ is the dynamic viscosity, considered to be a constant since we are dealing with a Newtonian fluid. The influence of the clot is captured through the third term on the right-hand side of the equation, where K_f is the hydraulic permeability of the clot [35]:

$$\frac{1}{K_f} = \frac{16}{\alpha^2} \tilde{F}_p^3 (1 + 56 \tilde{F}_p^3). \quad (9)$$

Here, $\tilde{F}_p = \min\left(\frac{1000}{1400}, \frac{F_p}{7000}\right)$ is the normalized concentration of fibrin polymer in the clot, considered to be bounded by value corresponding to the normal permeability of the clot, and α is the radius of the fibers.

We assume that blood plasma is driven by the pressure difference, and we set the pressure p_{in} at the inlet Γ_{in} and the pressure p_{out} at the outlet Γ_{out} . We consider no-slip boundary conditions $\mathbf{u} = \mathbf{0}$ at the other boundaries $\partial\Omega \setminus (\Gamma_{in} \cup \Gamma_{out})$. To set the inlet pressure in dependence on shear rate $\dot{\gamma}$, we use the formula $p_{in} = 4L\gamma\mu/D$, where L is the length of the vessel, and D is the diameter of the vessel. The outflow pressure is set to zero $p_{out} = 0$.

The reaction–diffusion system of the equation is solved numerically with a finite difference method and an upwinding scheme in discretizing convective terms in order to avoid numerical instabilities in the convection-dominated cases. A regular 160×20 mesh corresponding to a rectangular domain of a length equal to 8 mm and a height of 1 mm is

used in the numerical simulations. Accuracy of the results was controlled by decreasing the time and space steps in previous studies [14]. The model was implemented in C++ using an object-oriented architecture. The CPU time of a simulation corresponding to 1200 s of physical time is 8 min 34 s on a workstation with 16 cores and 64 GB of RAM.

2.2. The Artificial Neural Network for the Fast Prediction of the Coagulation Response

We used a workstation to run 7675 CFD simulations and generate the necessary data to train neural network models. To speed up the process, we ran eight simulations in parallel, where the parameters related to coagulability ($K_2, K_3, K_4, K_5, K_6, K_7, K_8, K_9, U^0$, and P^0), injury size (δ), and flow intensity (Δp) were randomly sampled from uniform distributions. For each simulation, we considered coagulation to be initiated if the height of the clot exceeds 50% of the vessel height. In this case, it continues growing until the vessel is completely obstructed. It is impossible to achieve a partial occlusion with the current model due to the absence of activated protein C. When coagulation is initiated, the clot first expands horizontally, leading to a decrease in flow velocity because of the constant pressure difference condition [14]. This, in turn, allows the clot to grow vertically and fully occlude the vessel. However, we stopped the simulation at this point to minimize the time of calculation. The areas occupied by the clot correspond to the locations where the fibrin polymer concentration exceeds 1000 nM. We labeled each simulation with a 1 if coagulation was initiated and with a 0 otherwise. We then calculated the lag time, endogenous thrombin potential (ETP), peak concentration, and time to peak by analyzing the thrombin generation curve, obtained by solving the system of factor X, prothrombin, and thrombin without diffusion and advection:

$$\frac{\partial U}{\partial t} = (K_1 + K_2 T + K_3 T^2)(U^0 - U) - K_4 U, \quad (10)$$

$$\frac{\partial T}{\partial t} = (K_5 U + K_6 T + K_7 T^2 + K_8 T^3)P - K_9 T, \quad (11)$$

$$\frac{\partial P}{\partial t} = -(K_5 U + K_6 T + K_7 T^2 + K_8 T^3)P. \quad (12)$$

This model describes the dynamics of thrombin generation in in vitro lab conditions, in the absence of flow velocity and diffusion. One important feature of this model is that it can reproduce the thrombin generation curves of real patients [36]. The mean and standard deviation of the ranges from which the parameters were sampled are shown in Table 1. The mean of these ranges corresponds to the parameter values of a healthy subject [36,37]. These data were collected in the clinical studies NCT02540187 and NCT02300519, which were approved by the French Ethical Review Board South East I. The subjects were included after having signed an informed consent form in accordance with the ethical principles of the Helsinki declaration. Since we are assuming the same tissue factor concentrations for all simulations, we also used the same K_1 for all of our calculations of thrombin generation curves. For each simulation, we only kept the four parameters of coagulability (lag time, ETP, thrombin peak concentration, and time to peak), in addition to the injury size (δ) and the pressure difference (Δp). We conducted a total of 7675 simulations and used 70% of the obtained dataset for the training of the neural network and 30% for testing its performance. The mean and standard deviation of the four coagulability parameters in the generated virtual patients population is given in Table 2. We used a neural network architecture that consists of three hidden layers of $500 \times 250 \times 100$ nodes (Figure 1). Initial values of weights were set with the uniform (Xavier) initialization [38]. The Adam learning rate optimization algorithm was used to fit the weights of the ANN [39].

Table 1. The mean and standard deviation of the parameters used in the simulations to generate the training dataset. The values of parameters related to coagulability were generated by considering the parameters of a real patient and adding a perturbation sampled from a uniform distribution [36], while we determined the average values of injury size and pressure difference according to the values used in in vitro experiments [1]. The radius of the interval of the uniform distribution used to sample the parameters is equal to 20% of the mean values.

Parameter	Mean	Standard Deviation
K_2	1.109932×10^{-5}	6.382294×10^{-7}
K_3	2.448583×10^{-7}	1.420816×10^{-8}
K_4	0.000479	0.000028
K_5	0.000019	0.000001
K_6	3.764441×10^{-6}	2.170468×10^{-7}
K_7	1.285508×10^{-10}	7.473447×10^{-12}
K_8	4.064636×10^{-10}	2.327669×10^{-11}
K_9	0.020216	0.001173
U^0	135.062467	14.774695
p^0	1401.066678	160.943197
Δp	135.062467	14.774695
δ	1401.066678	160.943197

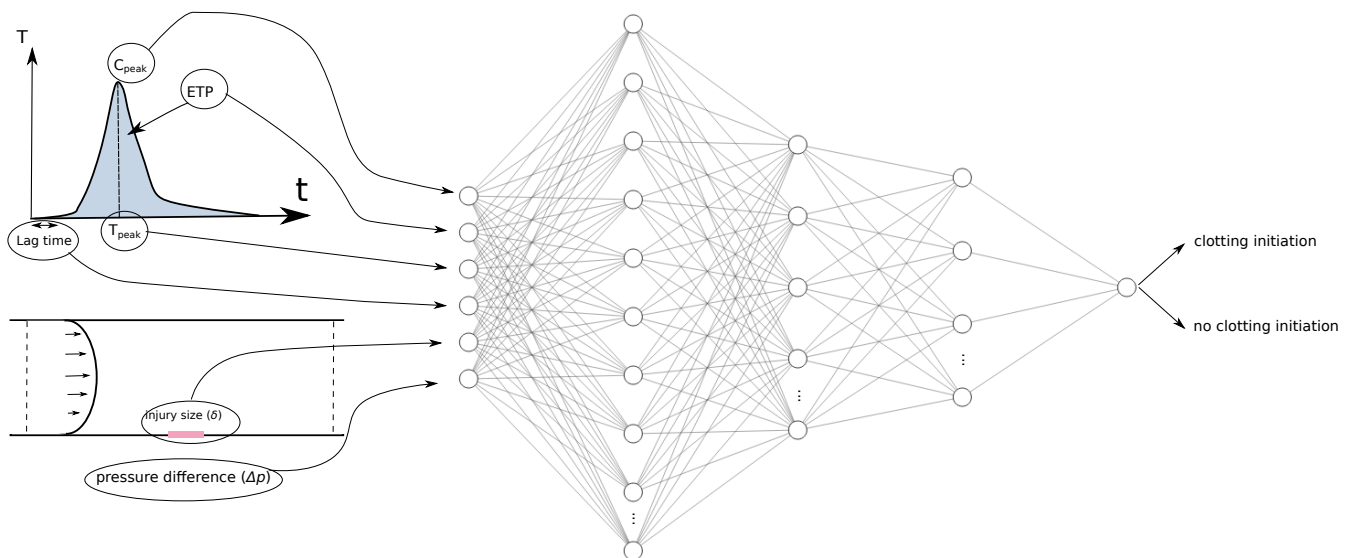


Figure 1. The architecture of the neural network used to predict the initiation of coagulation depending on coagulability, flow intensity, and injury site. The lag time, ETP, peak thrombin concentration, and time to peak were calculated for each thrombin generation curve, obtained by solving the system (10)–(12). To these parameters, we added the injury size and the flow intensity as inputs for the NN. We used an architecture that consists of three hidden layers, composed of $500 \times 250 \times 100$ nodes, chosen to prevent under- and over-fitting. In the output layer, we used one node that takes a value of 1 in the case where coagulation is initiated and 0 otherwise.

We trained the neural network for 200 periods and evaluated its performance by computing metrics such as the multi-cross entropy in log scale and the confusion matrix (Figure 2). Further, accuracy was evaluated at 94% on the test dataset. The performances of other NN architectures and classification algorithms are provided in Appendix A.2. To implement these algorithms, we used the Python libraries Scikit-learn [40] and tensorflow [41]. The database and the algorithm code are publicly available through the following github repository: https://github.com/MPS7/ML_coag (accessed on 8 August 2023).

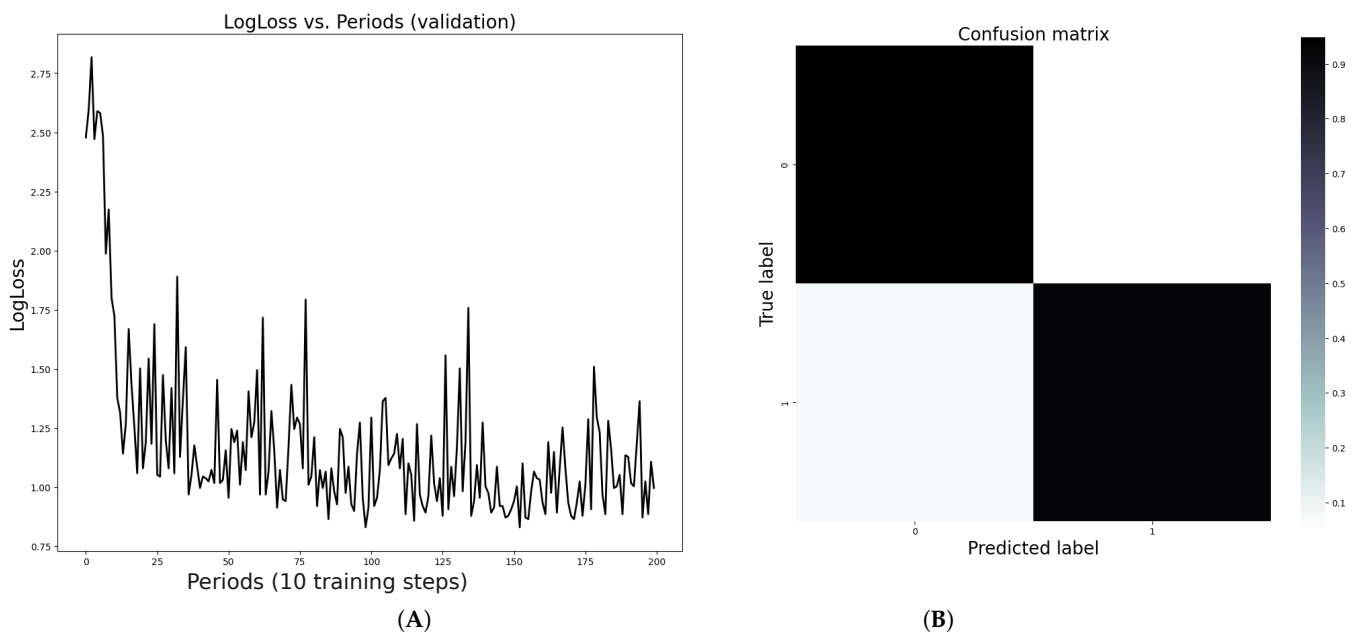


Figure 2. (A) Multi-cross entropy in log scale during training. The value of this metric was computed at the end of each period, consisting of 10 training steps. It measures how close the predictions of the model are to the actual test data. As loss decreases, the probability that the model predictions match the target value increases. (B) The confusion matrix measuring the classification precision of the ANN architecture. The confusion matrix represents the percentage of true and false predictions for each label.

Table 2. The mean and standard deviation of thrombin generation parameters calculated by solving the system (10)–(12) for each coagulability parameter set.

Parameter	Mean	Standard Deviation
lag time (min)	2.44537	0.3893
ETP (nM.min)	779.68770	169.85197
peak concentration (nM)	47.18947	12.6126
time to peak (nM)	26.19182	6.3149

3. Results

3.1. Model Calibration and Validation

We utilized the CFD thrombus growth model (Section 2.1) to study the initiation of clotting under flow by simulating in vitro experiments [1]. The experiment involved Newtonian flow of normal pooled plasma (NPP) through a tube with rigid walls, driven by a constant pressure drop. We ran numerical simulations for a physical time of 1200 s to determine the initiation time of blood coagulation, which corresponded to the start of the propagation phase where a sudden increase in the maximal value of generated fibrin polymer was observed near the tissue factor (TF) patch. This coincided with the time when the vessel became less permeable and the clot subsequently occluded the vessel. We controlled the initial shear rate by varying the pressure drop, and determined the value of the shear rate that prevented the initiation of coagulation by running consecutive simulations (Figure 3).

The concentration of TF expressed at the activation patch was varied to reproduce the results of experiments. In the default case where the patch size is 0.2 mm, the shear rate threshold which prevents coagulation initiation was estimated at $\approx 27.5 \text{ s}^{-1}$. We also conducted simulations where the TF patch size was changed. In the case where the patch size is small ($\delta = 0.1 \text{ mm}$), a shear rate equal to 12 s^{-1} was sufficient to prevent the initiation of coagulation, while a shear rate of 42.5 s^{-1} was required to stop clotting initiation when the size of the TF patch is higher ($\delta = 0.3 \text{ mm}$).

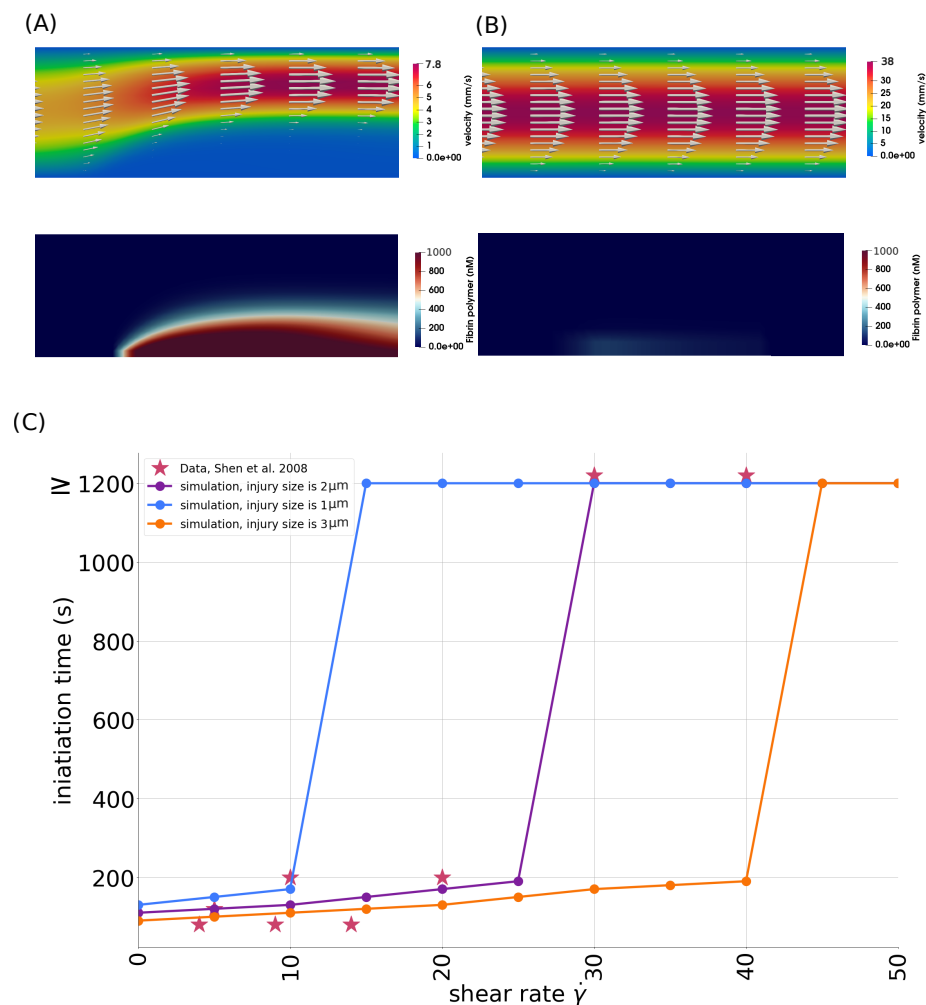


Figure 3. The initiation time of coagulation in the numerical simulations and comparison with experimental data [1]. The initiation time corresponds to the moment when the height of the clot reaches 20% of the vessel height. (A) Simulation snapshots showing the velocity profile and fibrin polymer concentration in the case where coagulation is initiated and the clot partially occludes the vessel. (B) Simulated flow velocity and fibrin polymer in the case where fast flow circulation prevents clot formation. (C) The initiation time in a series of simulations where the shear rate ($\dot{\gamma}$) and the injury size (δ) are varied. These results show that the threshold of shear rate which prevents clot formation depends on the size of the injury.

3.2. The Threshold of Coagulation Initiation under Flow in Hyper-Coagulable and Normal States

The threshold of coagulation initiation under flow corresponds to the level of shear stress or shear rate required to prevent the initiation of the coagulation cascade and the subsequent formation of a clot in flowing blood. In hypo-coagulable states, such as bleeding disorders or the presence of anticoagulants, it is expected that a lower threshold is necessary to prevent coagulation compared to normal states. This is because there are fewer procoagulant factors available to trigger the coagulation cascade. In contrast, in hyper-coagulable states, the shear rate threshold that prevents coagulation initiation is higher due to the presence of a sufficient amount of procoagulant factors that can readily initiate coagulation upon exposure to tissue factor or other triggers. We estimate this threshold for two cases corresponding to two values of the ETPs (Figure 4). In the case where ETP is normal (700 nM.min), the threshold of flow velocity that prevents coagulation corresponds to a shear rate of approximately $\dot{\gamma} = 28 \text{ s}^{-1}$ if the injury size is equal to 200 μm , while a higher threshold of $\dot{\gamma} = 37 \text{ s}^{-1}$ is required when the ETP corresponds to a hyper-coagulable state, for the same injury size value.

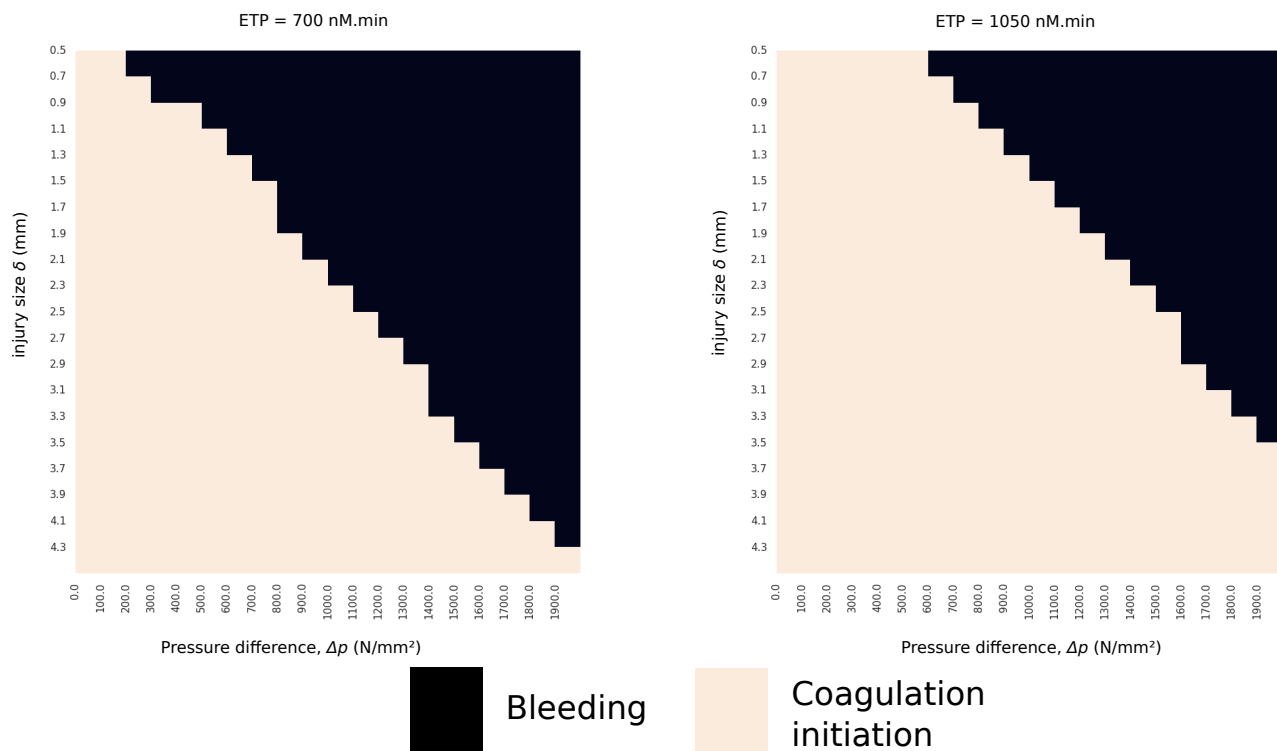


Figure 4. The threshold of coagulation initiation as a function of the pressure difference and injury size for a normal (left) and upregulated (right) value of the ETP. The black cases correspond to an absence of coagulation initiation, whereas the beige ones represent the cases where coagulation is initiated. The likelihood of coagulation initiation increases when the ETP is upregulated. Note that the increase of the injury size on the vertical axis is directed downwards.

3.3. The Threshold of ETP, Peak Concentration, and Time to Peak That Induces Clot Formation under Varying Flow Conditions

The balance between pro-coagulant and anti-coagulant forces determines thrombin generation. Four parameters, including the lag time, ETP, peak concentration, and time to peak, characterize the result of the TGA. However, it is challenging to evaluate the independent effect of each parameter on coagulation because clotting occurs in the presence of hemodynamic forces and injury size. Further, statistical analysis of thrombin generation parameters does not allow us to determine the effect of each of them, due to the dependencies between them.

Our surrogate models provide a means to examine the impact of each thrombin generation parameter on coagulation initiation, as depicted in Figure 5. We begin by studying the effect of the ETP parameter. Our estimates indicate that the threshold shear rate required to prevent coagulation initiation increases with an increase in ETP. Additionally, larger injury sizes further increase this threshold. The time to peak parameter describes the speed at which thrombin is generated, and an increase in this parameter causes a delay in thrombin generation dynamics. Our surrogate model suggests that, as the time to peak increases, the threshold shear rate required to prevent clotting decreases. This finding suggests that higher time to peak values correspond to a lower coagulability of the plasma. The peak concentration parameter increases the threshold flow intensity required to prevent coagulation initiation, indicating that elevated peak concentration can be linked to hyper-coagulable states. The lag time has approximately no effect on the shear rate threshold that prevents coagulation, especially for small injury size values.

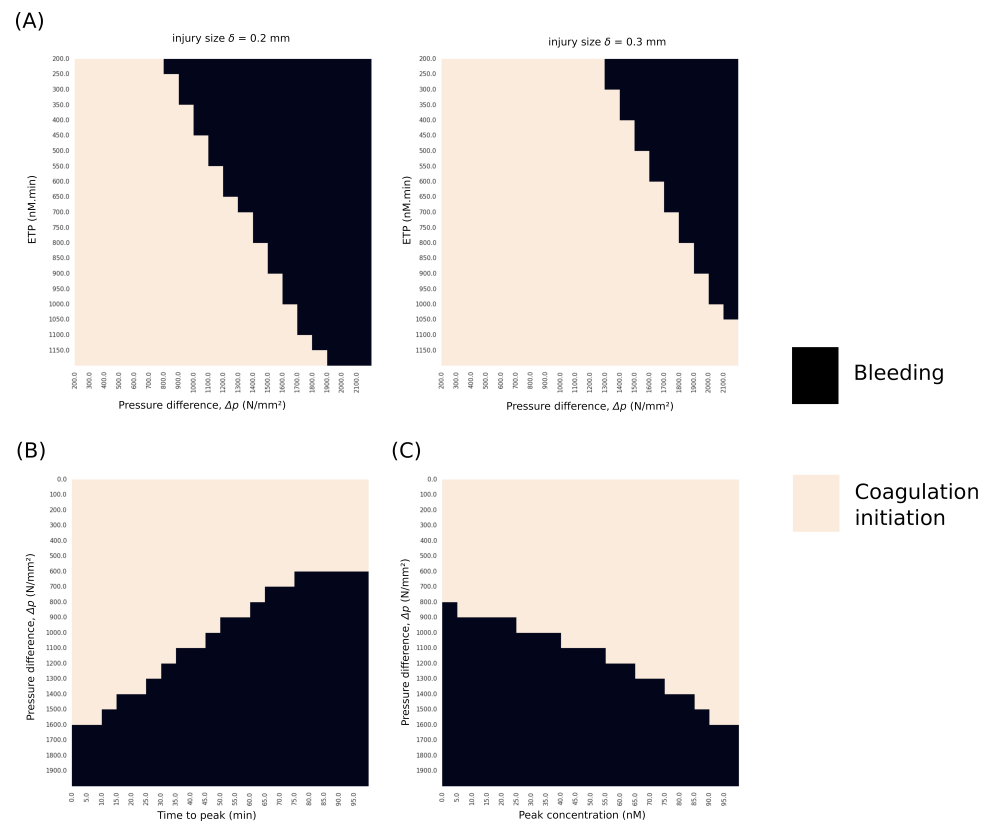


Figure 5. (A) The threshold of ETP under various flow conditions for two injury size values. (B) The threshold of the time to peak that stops coagulation initiation as a function of the flow intensity. (C) The threshold of peak concentration that leads to coagulation initiation for different values of pressure differences.

4. Discussion

This paper presents a new approach to explore the complex interplay between coagulation initiation thresholds in venous flow conditions. We utilized a previously developed CFD model to simulate the initiation of coagulation [13,14]. We calibrated our model to reproduce experimental observations and ran a large number of simulations to investigate the effects of blood coagulability, injury size, and flow intensity on coagulation initiation. We then post-processed the obtained dataset to calculate the thrombin generation parameters for each simulation, including the lag time, the ETP, the peak concentration, and the time to peak, which are crucial in quantifying plasma coagulability. By using an artificial neural network to analyze the post-processed dataset, we were able to predict the initiation of coagulation under varying coagulability, injury size, and flow intensity conditions. After training the model, we achieved a high accuracy of 94% on the test dataset, suggesting that the surrogate model can be used to effectively predict the outcome of simulations without resorting to the computationally intensive CFD model.

We took advantage of the accuracy of the surrogate model and its capacity to predict the outcome of coagulation initiation under a large number of conditions in a few seconds to study thresholds of thrombin generation parameters that alter the coagulation initiation dynamics. In particular, we were able to determine these thresholds for varying conditions of flow intensity and injury size. Our model predictions were in good agreement with the reported experimental findings in the literature. Indeed, it was shown experimentally that elevated ETP and peak concentrations values were associated with hypercoagulable states [42], while an increased time to peak was associated with poor coagulation [43,44]. It was also shown that the lag time has a minimal effect on coagulation, which also agrees with our model findings. These results indicate that ETP, peak concentration, and time to peak are the most reliable indicators of the likelihood of coagulation initiation.

Our study provides a robust and reliable framework for investigating the complex interplay between the components of the Virchow triad in a systemic way, and has the potential to contribute to the development of new strategies for preventing and treating thrombotic disorders. Still, it is important to note that the current implementation of the model relies on a few assumptions. First, the simulations that were used to calibrate the model were performed in *in vitro* settings. As a result, the application of this approach in clinical settings would require more validation against *in vivo* data. Second, our study does not consider the effect of platelets on coagulation. Since we are validating our model against experiments that utilize normal-pooled plasma, we decided to exclude platelets in the present study. However, we have studied their effects on the development of coagulation under venous flow in a previous study [13]. Third, the present study does not consider the effect of a complex blood rheology. This is because the experiments that we used for validation were performed with blood plasma, which displays a Newtonian rheology [1]. Finally, it is important to use the surrogate model to make predictions for parameter values within physiologically accepted ranges, although the model can provide predictions for non-physiological cases as well. For instance, it is impossible to have thrombin generation curves with peak concentrations equal to zero and a high endogenous thrombin potential. However, the surrogate model provides predictions for these values, as shown in Figure 5C.

The presented approach can serve as a basis for the development of a digital twin patient to design treatment for disorders of the hemostatic system. To achieve this, the model can be extended by including the effect of activated protein C, which localizes the clot. The effect of anticoagulant therapy can then be included using specific pharmacokinetics–pharmacodynamics models [31,45]. First, we must validate the framework’s utility by comparing its efficacy and safety to other assay methods in randomized clinical trials. In a forthcoming work, we will evaluate the effect of aerobic exercise on the risk of developing blood coagulation disorders using data collected from real subjects [46,47].

Author Contributions: Conceptualization, A.B. and V.V.; methodology, A.B., K.Y. and V.V.; software, A.B. and K.Y.; validation, J.-P.L., A.G. and V.V.; formal analysis, J.-P.L., A.G. and V.V.; investigation, A.B., K.Y., J.-P.L., A.G. and V.V.; resources, A.B.; data curation, A.B. and K.Y.; writing—original draft preparation, A.B. and K.Y.; writing—review and editing, J.-P.L., A.G. and V.V.; visualization, A.B. and K.Y.; supervision, A.B., J.-P.L., A.G. and V.V.; project administration, A.B.; funding acquisition, A.B. All authors have read and agreed to the published version of the manuscript.

Funding: V.V. was supported by the Ministry of Science and Higher Education of the Russian Federation (project number FSSF-2023-0016).

Data Availability Statement: All necessary equations, parameter values, and methods are reported in the manuscript. Data generated for the training of the machine learning algorithms are available on the repository https://github.com/MPS7/ML_coag (accessed on 8 August 2023).

Conflicts of Interest: The authors declare no conflict of interest.

Appendix A

Appendix A.1. Derivation of the Thrombin Generation Model

Let us consider a previously developed model to describe thrombin generation [48]:

$$\frac{\partial[Va]}{\partial t} = k_1T - h_1[Va], \quad (A1)$$

$$\frac{\partial[VIIIa]}{\partial t} = k_2T - h_2[VIIIa], \quad (A2)$$

$$\frac{\partial[XIa]}{\partial t} = k_3T - h_3[XIa], \quad (A3)$$

$$\frac{\partial[IXa]}{\partial t} = k_4[XIa] - h_4[IXa], \quad (A4)$$

$$\frac{\partial U}{\partial t} = (\bar{k}_5[TF] + k_5[XIa] + k_{55}[VIIIa][IXa])(U^0 - U) - h_5U, \quad (A5)$$

$$\frac{\partial T}{\partial t} = (k_6U + k_{66}U[Va])P - K_9T, \quad (A6)$$

where k_i denotes the activation coefficient rates and h_i the inhibition rates. The factors Va and Xa form the prothrombinase complex $Va - Xa$, while $VIIIa$ and IXa constitute the complex $VIIIa - IXa$. They are introduced in (A5) and (A6) in the form of the terms $k_{55}[VIIIa][IXa]$ and $k_{66}U[Va]$, obtained using the assumption of a detailed equilibrium for fast reactions. The concentrations of coagulation factors can be expressed as follows:

$$[Va] = \frac{k_1}{h_1}T, \quad [VIIIa] = \frac{k_2}{h_2}T, \quad [XIa] = \frac{k_3}{h_3}T, \quad [IXa] = \frac{k_3k_4}{h_3h_4}T, \quad (A7)$$

and assuming that Equation (A5) has reached equilibrium during the amplification phase ($\bar{k}_5[TF] = 0$ and considering a zero-order reaction instead of a first-order one), using the detailed equilibrium assumption, we obtain

$$[Xa] = \frac{k_3k_4}{h_3h_4}T \left(\frac{k_5}{h_5} + \frac{k_{55}k_2}{h_2h_5} \right). \quad (A8)$$

Substituting these concentrations with their expression in (A5) and (A6), we obtain two equations for factor XI (U) and thrombin (T), and we add to the system one equation for prothrombin (P):

$$\frac{\partial U}{\partial t} = (K_1 + K_2T + K_3T^2)(U^0 - U) - K_4U, \quad (A9)$$

$$\frac{\partial P}{\partial t} = -(K_5U + K_6T + K_7T^2 + K_8T^3)P, \quad (A10)$$

$$\frac{\partial T}{\partial t} = (K_5U + K_6T + K_7T^2 + K_8T^3)P - K_9T, \quad (A11)$$

where

$$\begin{aligned} K_1 &= \bar{k}_5[TF], \quad K_2 = \frac{k_5k_4k_3}{h_4h_3}, \quad K_3 = \frac{k_{55}k_2k_4k_3}{h_2h_4h_3}, \quad K_4 = h_5, \\ K_5 &= k_6, \quad K_6 = \frac{k_3k_4k_5k_6}{h_3h_4h_5}, \quad K_7 = \frac{k_2k_3k_4k_5k_6}{h_2h_3h_4h_5} + \frac{k_1k_3k_4k_5k_6}{h_1h_3h_4h_5}, \quad K_8 = \frac{k_1k_2k_3k_4k_5k_6}{h_1h_2h_3h_4h_5}. \end{aligned} \quad (A12)$$

These expressions are obtained by applying the detailed equilibrium approximation for fast reactions on the system (A1)–(A6). The reduced model gives a good approximation of the rate of clot growth described by the system (A1)–(A6) [49]. The nine parameters K_1, K_2, \dots, K_9 , as well as the concentrations of prothrombin (P_0) and factor Xa (U_0), can be fitted to approximate the thrombin generation curves of real patients [36]. The obtained model can be extended to determine the hemostatic response of patients under flow [31].

Appendix A.2. Performance Evaluation of Deep Learning Models

Figure A1 shows a comparison of the accuracies obtained using different classification methods on the same dataset. The evaluated methods include deep neural networks, support vector machines (SVMs) [50] with bagging and grid search, decision trees [51], XGBoost [52], and CatBoost [53]. We apply these algorithms to the same dataset that consists of the simulated coagulation initiation response under various parameters corresponding to flow characteristics, injury size, and blood coagulability.

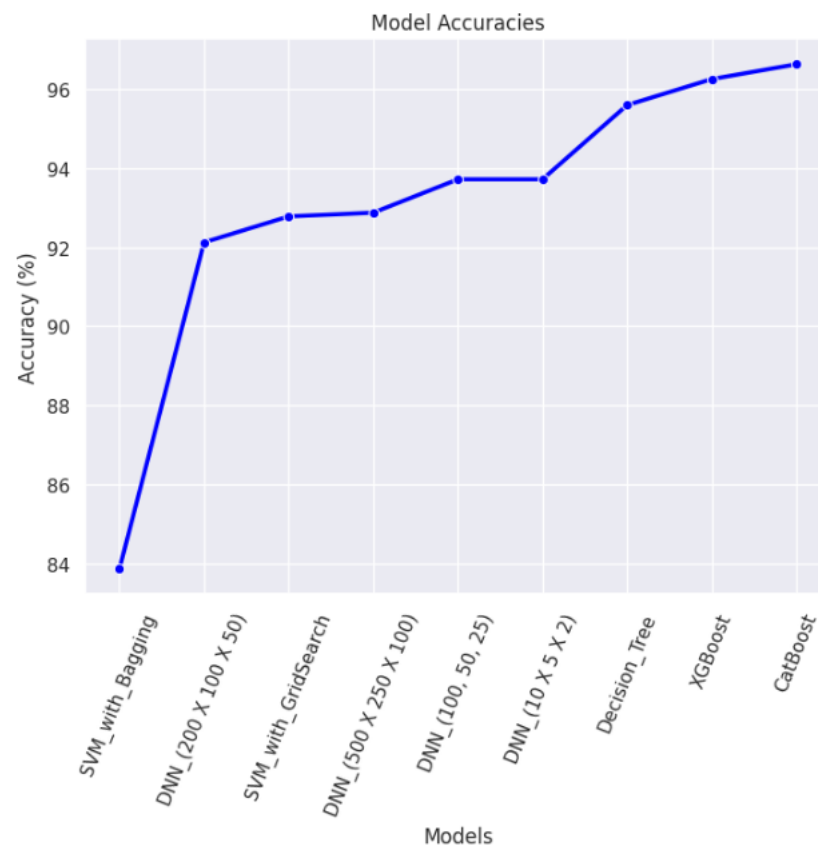


Figure A1. A comparison of the accuracies reached by the various classification algorithms when applied to the same coagulation initiation dataset.

We also evaluated the performance of four deep neural network architectures: $(500 \times 250 \times 100)$, $(200 \times 100 \times 50)$, $(100 \times 50 \times 25)$, and $(10 \times 5 \times 2)$. The accuracies obtained using these four architectures exceeded 90%. It further increases when simpler architectures are considered.

The performance of support vector machines was satisfactory as well, especially when grid search was used to determine the most suitable hyperparameters. A high accuracy was also obtained by decision tree algorithms. It exceeded 90% when the depth of the division tree was set to three levels. We opted for neural networks over traditional machine learning due to their proficiency with high-dimensional data, in anticipation of expansions that we plan to introduce in future studies.

Higher level boosting algorithms were also evaluated. Both the XGBoost and CatBoost algorithms yielded accuracies that were above 95%. Note that we have used the default values of the hyperparameters for these two algorithms. We decided to not use them for our main study to prevent over-fitting.

References

- Shen, F.; Kastrup, C.J.; Liu, Y.; Ismagilov, R.F. Threshold response of initiation of blood coagulation by tissue factor in patterned microfluidic capillaries is controlled by shear rate. *Arterioscler. Thromb. Vasc. Biol.* **2008**, *28*, 2035–2041. [\[CrossRef\]](#) [\[PubMed\]](#)
- Kastrup, C.J.; Shen, F.; Runyon, M.K.; Ismagilov, R.F. Characterization of the threshold response of initiation of blood clotting to stimulus patch size. *Biophys. J.* **2007**, *93*, 2969–2977. [\[CrossRef\]](#) [\[PubMed\]](#)
- Belyaev, A.V.; Panteleev, M.A.; Ataullakhanov, F.I. Threshold of microvascular occlusion: Injury size defines the thrombosis scenario. *Biophys. J.* **2015**, *109*, 450–456. [\[CrossRef\]](#) [\[PubMed\]](#)
- Louw, V.J.; Ntusi, N.A. Virchow's triad revisited. *S. Afr. Med. J.* **2019**, *109*, 822–823. [\[CrossRef\]](#)
- Castoldi, E.; Rosing, J. Thrombin generation tests. *Thromb. Res.* **2011**, *127*, S21–S25. [\[CrossRef\]](#) [\[PubMed\]](#)
- Ataullakhanov, F.; Guria, G.; Sarbash, V.; Volkova, R. Spatiotemporal dynamics of clotting and pattern formation in human blood. *Biochim. Biophys. Acta Gen. Subj.* **1998**, *1425*, 453–468. [\[CrossRef\]](#) [\[PubMed\]](#)

7. Brummel-Ziedins, K.E.; Orfeo, T.; Gissel, M.; Mann, K.G.; Rosendaal, F.R. Factor Xa generation by computational modeling: An additional discriminator to thrombin generation evaluation. *PLoS ONE* **2012**, *7*, e29178. [\[CrossRef\]](#)
8. Chatterjee, M.S.; Denney, W.S.; Jing, H.; Diamond, S.L. Systems biology of coagulation initiation: Kinetics of thrombin generation in resting and activated human blood. *PLoS Comput. Biol.* **2010**, *6*, e1000950. [\[CrossRef\]](#)
9. Jones, K.C.; Mann, K.G. A model for the tissue factor pathway to thrombin. II. A mathematical simulation. *J. Biol. Chem.* **1994**, *269*, 23367–23373. [\[CrossRef\]](#)
10. Anand, M.; Rajagopal, K.; Rajagopal, K. A model for the formation and lysis of blood clots. *Pathophysiol. Haemost. Thromb.* **2006**, *34*, 109–120. [\[CrossRef\]](#)
11. Heeb, M.J.; Mesters, R.; Tans, G.; Rosing, J.; Griffin, J. Binding of protein S to factor Va associated with inhibition of prothrombinase that is independent of activated protein C. *J. Biol. Chem.* **1993**, *268*, 2872–2877. [\[CrossRef\]](#) [\[PubMed\]](#)
12. Hemker, H.; Kerdelo, S.; Kremers, R. Is there value in kinetic modeling of thrombin generation? No (unless...). *J. Thromb. Haemost.* **2012**, *10*, 1470–1477. [\[CrossRef\]](#) [\[PubMed\]](#)
13. Bouchnita, A.; Terekhov, K.; Nony, P.; Vassilevski, Y.; Volpert, V. A mathematical model to quantify the effects of platelet count, shear rate, and injury size on the initiation of blood coagulation under venous flow conditions. *PLoS ONE* **2020**, *15*, e0235392. [\[CrossRef\]](#) [\[PubMed\]](#)
14. Bouchnita, A.; Galochkina, T.; Kurbatova, P.; Nony, P.; Volpert, V. Conditions of microvessel occlusion for blood coagulation in flow. *Int. J. Numer. Methods Biomed. Eng.* **2017**, *33*, e2850. [\[CrossRef\]](#) [\[PubMed\]](#)
15. Zheng, X.; Yazdani, A.; Li, H.; Humphrey, J.D.; Karniadakis, G.E. A three-dimensional phase-field model for multiscale modeling of thrombus biomechanics in blood vessels. *PLoS Comput. Biol.* **2020**, *16*, e1007709. [\[CrossRef\]](#) [\[PubMed\]](#)
16. Govindarajan, V.; Rakesh, V.; Reifman, J.; Mitrophanov, A.Y. Computational study of thrombus formation and clotting factor effects under venous flow conditions. *Biophys. J.* **2016**, *110*, 1869–1885. [\[CrossRef\]](#) [\[PubMed\]](#)
17. Leiderman, K.; Fogelson, A.L. Grow with the flow: A spatial-temporal model of platelet deposition and blood coagulation under flow. *Math. Med. Biol. J. IMA* **2011**, *28*, 47–84. [\[CrossRef\]](#) [\[PubMed\]](#)
18. Bodnár, T.; Sequeira, A. Numerical simulation of the coagulation dynamics of blood. *Comput. Math. Methods Med.* **2008**, *9*, 83–104. [\[CrossRef\]](#)
19. Wu, W.T.; Jamiolkowski, M.A.; Wagner, W.R.; Aubry, N.; Massoudi, M.; Antaki, J.F. Multi-constituent simulation of thrombus deposition. *Sci. Rep.* **2017**, *7*, 42720. [\[CrossRef\]](#)
20. Bouchnita, A.; Belyaev, A.V.; Volpert, V. Multiphase continuum modeling of thrombosis in aneurysms and recirculation zones. *Phys. Fluids* **2021**, *33*, 093314. [\[CrossRef\]](#)
21. Xu, S.; Xu, Z.; Kim, O.V.; Litvinov, R.I.; Weisel, J.W.; Alber, M. Model predictions of deformation, embolization and permeability of partially obstructive blood clots under variable shear flow. *J. R. Soc. Interface* **2017**, *14*, 20170441. [\[CrossRef\]](#) [\[PubMed\]](#)
22. Yazdani, A.; Deng, Y.; Li, H.; Javadi, E.; Li, Z.; Jamali, S.; Lin, C.; Humphrey, J.D.; Mantzoros, C.S.; Em Karniadakis, G. Integrating blood cell mechanics, platelet adhesive dynamics and coagulation cascade for modelling thrombus formation in normal and diabetic blood. *J. R. Soc. Interface* **2021**, *18*, 20200834. [\[CrossRef\]](#) [\[PubMed\]](#)
23. Yazdani, A.; Li, H.; Humphrey, J.D.; Karniadakis, G.E. A general shear-dependent model for thrombus formation. *PLoS Comput. Biol.* **2017**, *13*, e1005291. [\[CrossRef\]](#) [\[PubMed\]](#)
24. Tosenberger, A.; Ataulakhanov, F.; Bessonov, N.; Pantelev, M.; Tokarev, A.; Volpert, V. Modelling of thrombus growth in flow with a DPD-PDE method. *J. Theor. Biol.* **2013**, *337*, 30–41. [\[CrossRef\]](#) [\[PubMed\]](#)
25. Fogelson, A.L.; Guy, R.D. Immersed-boundary-type models of intravascular platelet aggregation. *Comput. Methods Appl. Mech. Eng.* **2008**, *197*, 2087–2104. [\[CrossRef\]](#)
26. Bouchnita, A.; Volpert, V. A multiscale model of platelet-fibrin thrombus growth in the flow. *Comput. Fluids* **2019**, *184*, 10–20. [\[CrossRef\]](#)
27. Tsyu, N.G.; Belyaev, A.V. Coarse-grained simulations of von Willebrand factor adsorption to collagen with consequent platelet recruitment. *Int. J. Numer. Methods Biomed. Eng.* **2023**, e3747. [\[CrossRef\]](#)
28. Shankar, K.N.; Zhang, Y.; Sinno, T.; Diamond, S.L. A three-dimensional multiscale model for the prediction of thrombus growth under flow with single-platelet resolution. *PLoS Comput. Biol.* **2022**, *18*, e1009850. [\[CrossRef\]](#)
29. Yoon, J.G.; Heo, J.; Kim, M.; Park, Y.J.; Choi, M.H.; Song, J.; Wyi, K.; Kim, H.; Duchenne, O.; Eom, S.; et al. Machine learning-based diagnosis for disseminated intravascular coagulation (DIC): Development, external validation, and comparison to scoring systems. *PLoS ONE* **2018**, *13*, e0195861. [\[CrossRef\]](#)
30. Fang, K.; Dong, Z.; Chen, X.; Zhu, J.; Zhang, B.; You, J.; Xiao, Y.; Xia, W. Using machine learning to identify clotted specimens in coagulation testing. *Clin. Chem. Lab. Med.* **2021**, *59*, 1289–1297. [\[CrossRef\]](#)
31. Bouchnita, A.; Nony, P.; Llored, J.P.; Volpert, V. Combining mathematical modeling and deep learning to make rapid and explainable predictions of the patient-specific response to anticoagulant therapy under venous flow. *Math. Biosci.* **2022**, *349*, 108830. [\[CrossRef\]](#) [\[PubMed\]](#)
32. Bouchnita, A.; Mozokhina, A.; Nony, P.; Llored, J.P.; Volpert, V. Combining Computational Modelling and Machine Learning to Identify COVID-19 Patients with a High Thromboembolism Risk. *Mathematics* **2023**, *11*, 289. [\[CrossRef\]](#)
33. Brummel-Ziedins, K. Models for thrombin generation and risk of disease. *J. Thromb. Haemost.* **2013**, *11*, 212–223. [\[PubMed\]](#)
34. Danforth, C.M.; Orfeo, T.; Everse, S.J.; Mann, K.G.; Brummel-Ziedins, K.E. Defining the boundaries of normal thrombin generation: Investigations into hemostasis. *PLoS ONE* **2012**, *7*, e30385. [\[CrossRef\]](#) [\[PubMed\]](#)

35. Wufsus, A.R.; Macera, N.; Neeves, K. The hydraulic permeability of blood clots as a function of fibrin and platelet density. *Biophys. J.* **2013**, *104*, 1812–1823. [[CrossRef](#)] [[PubMed](#)]
36. Ratto, N.; Tokarev, A.; Chelle, P.; Tardy-Poncet, B.; Volpert, V. Clustering of thrombin generation test data using a reduced mathematical model of blood coagulation. *Acta Biotheor.* **2020**, *68*, 21–43. [[CrossRef](#)] [[PubMed](#)]
37. Ratto, N.; Bouchnita, A.; Chelle, P.; Marion, M.; Panteleev, M.; Nechipurenko, D.; Tardy-Poncet, B.; Volpert, V. Patient-specific modelling of blood coagulation. *Bull. Math. Biol.* **2021**, *83*, 50. [[CrossRef](#)] [[PubMed](#)]
38. Glorot, X.; Bengio, Y. Understanding the difficulty of training deep feedforward neural networks. In Proceedings of the Thirteenth International Conference on Artificial Intelligence and Statistics, Sardinia, Italy, 13–15 May 2010; pp. 249–256.
39. Kingma, D.P.; Ba, J. Adam: A method for stochastic optimization. *arXiv* **2014**, arXiv:1412.6980.
40. Pedregosa, F.; Varoquaux, G.; Gramfort, A.; Michel, V.; Thirion, B.; Grisel, O.; Blondel, M.; Prettenhofer, P.; Weiss, R.; Dubourg, V.; et al. Scikit-learn: Machine learning in Python. *J. Mach. Learn. Res.* **2011**, *12*, 2825–2830.
41. Abadi, M.; Barham, P.; Chen, J.; Chen, Z.; Davis, A.; Dean, J.; Devin, M.; Ghemawat, S.; Irving, G.; Isard, M.; et al. Tensorflow: A system for large-scale machine learning. In Proceedings of the OSDI, Savannah, GA, USA, 2–4 November 2016; Volume 16, pp. 265–283.
42. Binder, N.B.; Depasse, F.; Mueller, J.; Wissel, T.; Schwes, S.; Germer, M.; Hermes, B.; Turecek, P.L. Clinical use of thrombin generation assays. *J. Thromb. Haemost.* **2021**, *19*, 2918–2929. [[CrossRef](#)]
43. Zavyalova, E.; Kopylov, A. Exploring potential anticoagulant drug formulations using thrombin generation test. *Biochem. Biophys. Rep.* **2016**, *5*, 111–119. [[CrossRef](#)] [[PubMed](#)]
44. Tripodi, A. Thrombin generation: A global coagulation procedure to investigate hypo- and hyper-coagulability. *Haematologica* **2020**, *105*, 2196. [[CrossRef](#)] [[PubMed](#)]
45. Bouchnita, A.; Bouzaachane, K.; Galochkina, T.; Kurbatova, P.; Nony, P.; Volpert, V. An individualized blood coagulation model to predict INR therapeutic range during warfarin treatment. *Math. Model. Nat. Phenom.* **2016**, *11*, 28–44. [[CrossRef](#)]
46. Montalvo, S.; Gomez, M.; Lozano, A.; Arias, S.; Rodriguez, L.; Morales-Acuna, F.; Gurovich, A.N. Differences in blood flow patterns and endothelial shear stress at the carotid artery using different exercise modalities and intensities. *Front. Physiol.* **2022**, *13*, 922. [[CrossRef](#)] [[PubMed](#)]
47. Gurovich, A.N.; Rodriguez, L.; Morales-Acuna, F. There are no differences in brachial artery endothelial shear stress and blood flow patterns between males and females during exercise. *Clin. Physiol. Funct. Imaging* **2021**, *41*, 471–479. [[CrossRef](#)] [[PubMed](#)]
48. Krasotkina, Y.V.; Sinauridze, E.I.; Ataullakhanov, F.I. Spatiotemporal dynamics of fibrin formation and spreading of active thrombin entering non-recalcified plasma by diffusion. *Biochim. Biophys. Acta Gen. Subj.* **2000**, *1474*, 337–345. [[CrossRef](#)]
49. Galochkina, T.; Bouchnita, A.; Kurbatova, P.; Volpert, V. Reaction-diffusion waves of blood coagulation. *Math. Biosci.* **2017**, *288*, 130–139. [[CrossRef](#)]
50. Sain, S.R. The nature of statistical learning theory. *Technometrics* **1996**, *38*, 409. [[CrossRef](#)]
51. Song, Y.Y.; Ying, L. Decision tree methods: Applications for classification and prediction. *Shanghai Arch. Psychiatry* **2015**, *27*, 130.
52. Chen, T.; Guestrin, C. XGBoost: A scalable tree boosting system. In Proceedings of the 22nd ACM SIGKDD International Conference on Knowledge Discovery and Data Mining, San Francisco, CA, USA, 13–17 August 2016; pp. 785–794.
53. Hancock, J.T.; Khoshgoftaar, T.M. CatBoost for big data: An interdisciplinary review. *J. Big Data* **2020**, *7*, 94. [[CrossRef](#)]

Disclaimer/Publisher’s Note: The statements, opinions and data contained in all publications are solely those of the individual author(s) and contributor(s) and not of MDPI and/or the editor(s). MDPI and/or the editor(s) disclaim responsibility for any injury to people or property resulting from any ideas, methods, instructions or products referred to in the content.